Journal of Applied Physics

AIP Publishing

A Machine Learning Approach to Predicting the Spall Strength of Metals and Alloys

Keara G. Frawley[1], Naresh N. Thadhani[1], Rampi Ramprasad[1], Harikrishna Sahu[1*]
[1]School of Materials Science and Engineering, Georgia Institute of Technology, 771 Ferst Drive NW, Atlanta, 30332, GA, United States

*Corresponding author. E-mail:
hsahu3@gatech.edu

Abstract

Spall strength is a critical property that characterizes a material's resistance to dynamic failure under impact or shock-compression loading. Accurate prediction and control of spall strength are essential for designing materials used in armor, vehicle components, structural barriers, and mining. Traditional methods for measuring the spall strength are slow, destructive, and expensive, while existing models offer limited predictive accuracy. This study introduces a machine learning (ML) regression model that rapidly and accurately predicts the spall strength of metals and alloys at strain rates in the range of 10^5 to 10^6 s^{-1}. Trained on a dataset of over 70 metals and alloys and validated with recent data, the model identifies tensile yield strength and bulk modulus as key factors, with higher values of these properties correlating with increased spall strength. The findings offer an efficient method for screening metals and alloys and guiding the selection of high-spall-strength candidates for targeted experimental validation.

1. Introduction

Dynamic tensile strength, also known as spall strength, measures a material's resistance to internal failure under high-velocity impacts and explosive forces.[1] It plays a crucial role in the design and performance of armor, vehicle components, structural barriers, and mining operations.[2–5] Spall failure occurs through void or crack nucleation, growth, and coalescence due to the buildup of internal tension caused by wave reflections associated with high-pressure and high-strain-rate impact.

Spall strength is typically measured using planar parallel plate-on-plate impact experiments. Shock waves generated upon impact travel through the plates and reflect off free surfaces, producing rarefaction (release) waves. The interaction of these waves leads to the buildup of internal tensile stresses, causing spall failure if the material's tensile strength is exceeded.[2,3,6] Shock compression preceding the build-up of tension can induce plastic deformation at strain rates exceeding 10^5 s^{-1}, which increases with applied stress. The deformation can alter the pre-existing microstructure through competing processes of slip-dominated dislocation motion (influenced by thermal activation or viscous drag), twinning, or even martensitic transformation.[6–8]

Measuring spall strength is both time-consuming and costly, and results in sample destruction.[9] The need for time-resolved measurements commonly used in these experiments add further complexity. Although the spallation process is fairly well understood, as detailed in several review articles,[1,10,11] predicting spall strength across a broad range of metals and alloys remains challenging. This difficulty arises from the vast diversity of materials, their inherent ductile or brittle behaviors, and the shock-compression induced microstructural changes that precede and influence spall failure.

Grady's[12] energy-balancing approach provides a method for predicting spall strength by considering the equilibrium between elastic strain energy and material cohesive energy. The approach leverages the disparity between brittle and ductile material failures to formulate equations for theoretical spall strength. The knowledge of the ductile or brittle nature of the material, however, is possible through post-mortem fractographic analysis that may not always be feasible. Cochran and Banner[13] developed a predictive spall model, utilizing void nucleation and growth processes of spall damage to simulate and correlate with the measured free surface temporal evolution or velocity profile to enable spall strength determination. Initially based on experiments with uranium, the model has been tested on a few other metals. A modified version

of the Cochran-Banner model,[14] incorporating redefined damage parameters, has been shown to closely replicate experimentally determined spall strengths for copper, steel, and uranium. Calculating damage, however, remains computationally expensive and complex, as it requires in-depth understanding of the shock compression behavior of the material.

Machine learning (ML) has emerged as a powerful and efficient tool for developing predictive models for a wide range of material properties, including microstructure-dependent mechanical properties. Xiong et al.[15] utilized a database of 360 different steels to build five ML models to predict fatigue strength, tensile strength, fracture strength, and hardness. Stoll and Benner[16] employed small punch test data to predict the ultimate tensile strength (UTS) of steels using both linear and random forest models, utilizing values obtained from the load-displacement curve as characteristic features. Agrawal et al.[17] predicted the fatigue life of steels based on chemical composition, upstream processing details, heat treatment conditions, and mechanical properties through ML techniques. ML has also been applied to model spall fracture mechanisms. For example, Mayer and Pogorelko et al.[18] modeled the spall fracture of copper by performing molecular dynamics (MD) simulations and using an ML algorithm to optimize model parameters. They investigated strain-rate dependence of spall strength on initial defects like pores and how they evolve over time. In another study, Mayer and Lekanov et al.[19] explored the deformation behavior of copper under high strain rates and severe strains during spall failure, integrating MD data into an ML model. Blaschke et al.[20] used ML techniques to generate parameters for a model representing ductile failure in copper and an aluminum alloy, eliminating the need for experimental parameter generation. Mayer developed a machine learning model to predict the spall strength of aluminum, incorporating the effects of preliminary deformation and the resulting microstructural changes.[21] Despite these advancements, no existing ML model predicts spall strength across a broad range of metals and alloys using intrinsic, readily available material properties. Current models either rely on computationally intensive calculations of material failure parameters or lack the precision needed to accurately predict spall strength values.

In this study, an ML model was developed to predict the spall strengths of 73 metals and alloys. The model leverages key material properties that influence compressibility during initial shock compression, plastic flow strength (measure of resistance to permanent deformation from tensile forces), and fracture toughness (related to material failure and rupture following growth of cracks). These properties are hypothesized to influence spall strength and are therefore used as

features for prediction. The approach, illustrated in Figure 1, begins by identifying a dataset of easily accessible features related to spall strength. A regression model is then constructed using the Gaussian Process Regression (GPR) algorithm[22] based on these features. The resulting model is employed to evaluate materials with spall strengths that are recently published or have not been published at all, followed by the extraction of predictive guidelines through model analysis.

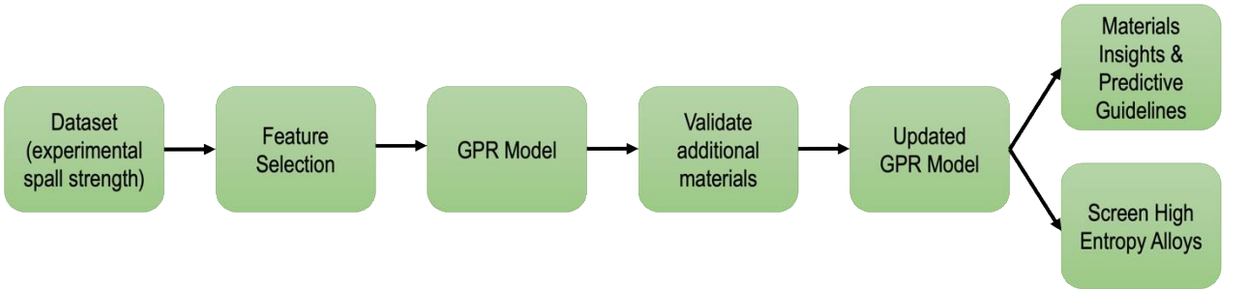

Figure 1: Workflow for developing the ML model and creating rules for predicting spall strengths of metals and alloys.

2. Dataset and Methodology

A compilation of the reported data of spall strength values for metals and alloys is presented in this section, along with properties that are expected to be correlated to spall strength. A physically-based model previously used to compute the theoretical spall strength for metals and alloys with ductile/brittle considerations is then described, followed by the methodology used here for development of the ML model.

2.1 Dataset of Spall Strengths and Features

The dataset of spall strength values of 73 metals and alloys was collected from literature, and also obtained from prior experiments conducted in our high-strain rate laboratory at Georgia Tech.[23–25] All spall strength values are exclusively those obtained from plate-on-plate impact experiments using gun- or explosively-launched projectiles, where strain rates range from 10^5 to 10^6 s^{-1} and shock wave duration is approximately 1 μs. Spall strength values obtained from other methods, such as explosively generated shock waves, directed energy lasers, or laser-launched thin foil impact experiments—where strain rates exceed 10^7 s^{-1}—were excluded from this study. This is because spall strengths at these higher strain rates are significantly elevated due to variations in the kinetic response of materials during spall failure.[26] At different strain rates, fracture modes can also change, further influencing the spall strength of the material.[27] Values of the spall strength (σ_{sp}) used in the dataset were obtained either directly through measurements of stress profile with

use of stress gauges, or calculated from pullback velocities measured using interferometry techniques like VISAR or PDV using the following equation:

$$\sigma_{sp} = \frac{1}{2}\rho_0 C_0 \Delta u_{fs} \quad \text{(Eq. 1)}$$

Where ρ_0 is the density, C_0 is the bulk sound speed, and Δu_{fs} is the change in the free surface velocity caused by tensile pullback due to generation of free surface.

Figure 2 displays the distribution of spall strength values for all metals and alloys included in the dataset (listed in Table S1). The dataset consists of 20 unique metals and 53 unique alloys, including iron-based alloys and steels (16 instances), aluminum and its alloys (13 instances), copper and its alloys (8 instances), nickel and its alloys (6 instances) and titanium and its alloys (5 instances). Spall strength median values range from 0.36 GPa for Cu-10Ta to 5.77 GPa for Stainless Steel 2169. The four highest spall strength values are observed in specialty steels: Stainless Steel 2169, AF 9628, AISI Steel 4340, and Duplex Stainless Steel 2205.

Alloys subjected to different heat treatments are treated as separate entries in the dataset due to the variations in spall strength and their other feature values. When multiple data points were available for a given material, either due to differences in experimental conditions, or data from various literature sources, the median value was used for consistency, with the variance in spall strength represented by vertical bars in Figure 2. For example, the spall strength of Al 6061-T6 ranges from 0.8 to 2.3 GPa, owing to variations in impactor thickness, impact velocity, and other conditions. Similarly, AISI 1020 steel shows a spall strength range of 1.6 to 3.5 GPa due to experiments conducted under different impact stresses. Commercial purity titanium and Ti-6Al-4V exhibit spall strength spreads of 2.1 to 3.9 GPa and 3.3 to 4.9 GPa, respectively, again influenced by varying experimental conditions across different laboratories.

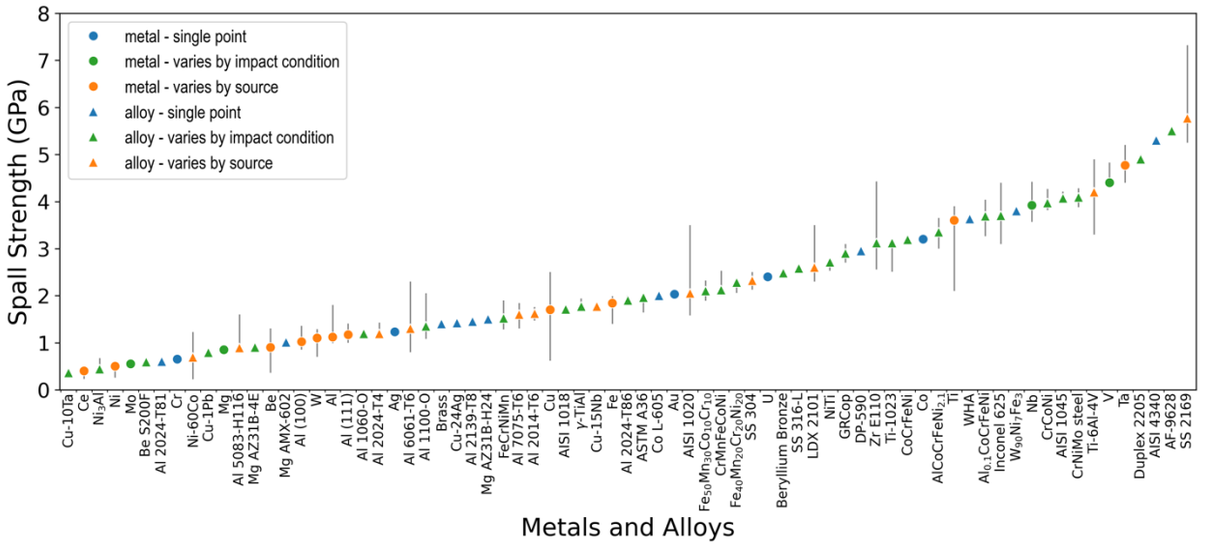

Figure 2: Median spall strength values for commercial purity metals (circles) and alloys (triangles). Colors indicate data types: singular data points (green), impact condition-dependent values (orange), and values varying by literature source (blue). Vertical bars represent the range for points with multiple values.

The selection of features in this study is informed by the mechanisms driving spall failure,[28] which is preceded by compression from impact-induced shock loading[29] prior to the build-up of internal tensile stresses exceeding the material's strength. Since the mechanical properties of metals and alloys are influenced by their microstructure, shaped by thermomechanical processing during fabrication, this work assumes—and tests—that intrinsic elastic and extrinsic mechanical properties capture these effects, in line with the process-structure-property-performance paradigm. Key features influencing compressibility and wave propagation velocity during shock loading include material density and stiffness, represented by bulk, shear, and elastic moduli. The tensile and compressive yield strengths, ultimate tensile strength, and hardness represent the material's resistance to plastic deformation. Combined with fracture toughness, these properties represent the ability of materials to resist internal failure through void nucleation, growth, and coalescence processes. The selected features collectively capture the essential characteristics of materials relevant to spallation, consistent with Grady's predictive model,[12] providing a foundation for developing the ML-enabled model critical for material predictive guidelines and evaluation.

Figure 3 illustrates the correlation between spall strength and each of the nine features selected for analysis: ultimate tensile strength (UTS), tensile yield strength, compressive yield strength, fracture toughness, hardness, density, bulk modulus, shear modulus, and Young's modulus (listed in Table S1). It is worth noting that although all three moduli are considered, for

isotropic elastic bodies, such as polycrystalline metals, only two independent moduli are required. Later in this work, we determine which two of the three are best suited for the model.

For consistency, when multiple data points were available for a given material, the median value and range were used, as mentioned before. Each plot in Figure 3 is annotated with the Pearson correlation coefficient (r), for the linear relationship between the corresponding property and spall strength. Notably, UTS and tensile yield strength exhibit correlations greater than 0.5, despite some scatter. While these properties are relevant to spall failure under dynamic loading, no single property or combination of properties reliably predicts spall strength, as confirmed by the linear regression analysis shown in the parity plot in Figure S1.

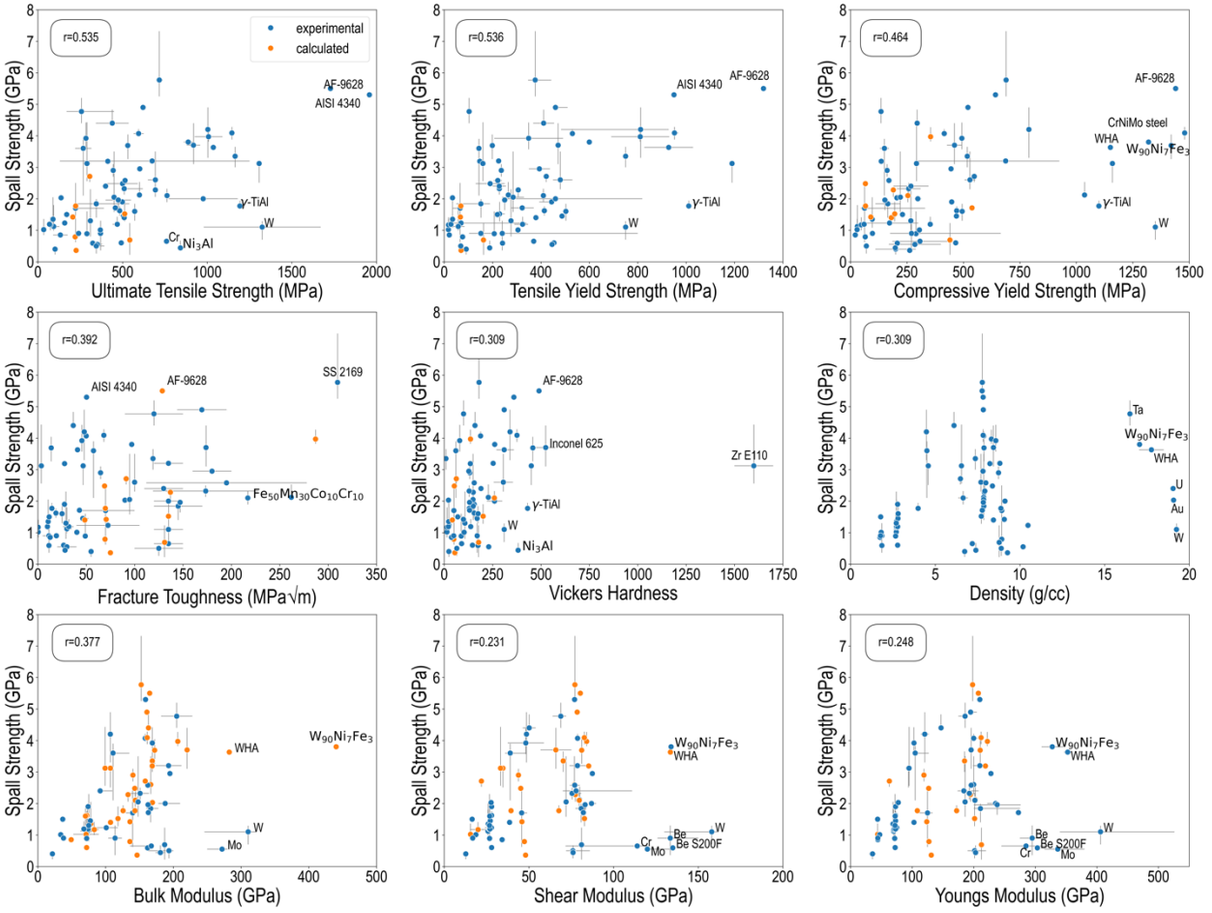

Figure 3: Median spall strength and feature values with their Pearson correlation coefficient (r). The calculated values (orange) are not directly from literature, unlike the non-calculated values (blue). Values have been calculated from various equations, including the rule of mixtures and the relationships between elastic moduli. The vertical and horizontal bars indicate the range of values for those with multiple data sources.

2.2 Grady's Theoretical Spall Strength Model

Grady[12] developed a model to predict the theoretical spall strength of both brittle and ductile metals and alloys. The model considers potential and kinetic energy constraints associated with tensile loads exceeding the fracture energy and the balance between work done and energy dissipation in activation, growth, and coalescence of spall-induced crack/voids. The theoretical spall strength (P_s) of brittle materials failing through linking of a network of cracks, is represented by the equation:

$$P_s = (3\rho c_0 K_c^2 \dot{\varepsilon})^{1/3} \quad \text{(Eq. 2)}$$

Where ρc_0^2 is the compressibility defined by bulk modulus, K_c is the fracture toughness, and $\dot{\varepsilon}$ is the volumetric strain rate.

In contrast, the theoretical spall strength of ductile materials is represented by the equation:

$$P_s = (2\rho c_0^2 Y \varepsilon_c)^{1/2} \quad \text{(Eq. 3)}$$

where Y is the flow stress and ε_c is the critical void volume fraction, which is typically found to be $\varepsilon_c = 0.15$ for most metals and alloys. As an example, the theoretical and experimental values of spall strengths of commercial grade Ti (considered a brittle material) are reported by Grady as 1.6 to 3.4 GPa and 2.1 to 3.9 GPa, respectively. For Ta (considered a ductile material), the corresponding values are given as 6.5 GPa and 4.4 to 6.8 GPa, respectively. Grady's model was extended to predict the theoretical spall strengths of all metals and alloys considered in this work and correlated with their corresponding experimental values.

2.3 Machine Learning Models

This study utilized the ML model based on Gaussian Process Regression (GPR) with a radial basis function (RBF) kernel. Model training and predictions were executed using the GPR implementation from the scikit-learn library.[30] GPR is a non-parametric Bayesian approach used for regression tasks. Its key principles include prior distribution, Bayesian inference, and uncertainty quantification. A Gaussian process defines a distribution over functions, characterized by a mean function and a covariance function (kernel), which captures relationships between data points. Given any observed data, GPR updates the function estimation, producing a posterior distribution that reflects both prior knowledge and observed data. Hence, GPR can provide not only predictions but also confidence intervals, making it particularly useful for modeling uncertainty in spall strength predictions.

The covariance function between two materials with features x and x' is defined as:

$$k(x, x') = \sigma_f \exp\left(-\frac{1}{2\sigma_l^2}\left|\left|x - x'\right|\right|^2\right) + \sigma_n^2 \text{.....(Eq. 4)}$$

where the three hyperparameters σ_f, σ_l, and σ_n represent the variance, the length-scale parameter, and the expected noise in the data, respectively. These hyperparameters were optimized during the model training process. To evaluate the predictive performance of the model, four key error metrics were employed: the standard deviation, the coefficient of determination (R^2), the Pearson correlation coefficient (r), and the root mean square error ($RMSE$). In GPR, the standard deviation at a point is computed from the model's predictive variance, reflecting uncertainty from the model's learned structure and distances to training data. Together, these metrics provide insights into the accuracy and reliability of the model's predictions relative to the actual spall strength values.[31]

The ML models were trained using a 90-10 train-test split, ensuring that the test set consisted of materials different from those in the training set. This approach allowed for evaluation on unseen cases. The model optimization process utilized a grid search to fine-tune hyperparameters, coupled with 3-fold cross-validation[32] (CV) to enhance robustness and generalizability. In 3-fold CV, the dataset is partitioned into three subsets. Each subset is sequentially held out as a test set while the model is trained on the remaining two, ensuring that every data point is used for both training and validation. This approach helps mitigate overfitting and provides a more reliable assessment of model performance. Once the hyperparameters were optimized, two production models were developed. The first production model was validated using three previously unseen candidates (recently investigated materials), demonstrating its ability to generalize beyond the training data. After successful validation, these candidates were incorporated into the dataset to train the final production model using 100% of the available data. To ensure reliability, all models, including the final production model, underwent a rigorous 3-fold cross-validation process, reinforcing robust hyperparameter tuning and evaluation.

Initially, we considered all nine potential features when building the ML models. Although using all nine properties yielded satisfactory results, we aimed to determine whether all were necessary. The objective was to achieve optimal model performance with the fewest features, in

order to improve efficiency and reduce costs. Consequently, we developed multiple models, testing various combinations and numbers of features. To further refine our feature selection, we conducted correlation analyses on the features we hypothesized to be most similar, e.g., the three strengths and the three elastic moduli. As expected, there is a high correlation between the three strengths and the three moduli (Figure S2), suggesting that it may not be necessary to include all three from each category. We found that removing the compressive yield strength and shear modulus resulted in only a minimal decrease in model performance, allowing us to reduce the total number of features from nine to seven, as presented in Figure S3. Therefore, the models presented here forth utilize the following seven features: UTS, tensile yield strength, fracture toughness, hardness, density, bulk modulus, and Young's modulus.

3. Model Results

We first present the results of the theoretical spall strengths of metals and alloys calculated using Grady's model and correlate those with the corresponding experimentally measured values reported in the literature. Next, the development of the ML model is presented along with its validation, reliability for different classes of materials, statistical analysis for model prediction, and application with insights and guidelines for predicting spall strength for a complex alloys system.

3.1 Grady's Theoretical Spall Strength Model

Grady's model was used to calculate the "theoretical" spall strength of metals and alloys by classifying them as either brittle or ductile. Metallic materials with a fracture toughness of 40 MPa$\sqrt{\text{m}}$ or higher generally exhibit ductile failure characteristics, while those with lower values are often considered as being brittle. Using this as the categorization of brittle and ductile behaviors, we calculated the theoretical spall strength values using the corresponding equations (2) and (3). Figure 4 shows the calculated "theoretical" spall strength values plotted against the actual measured values for the full range of materials considered in this work. The range in ductile values, indicated by purple vertical bars, reflects the variability in yield stress, while for brittle materials, the range (green vertical bars) corresponds to calculations based on strain rates of 2×10^4 and 2×10^5 s^{-1}, consistent with the criteria used by Grady. The negative R^2 and high $RMSE$ values for both ductile and brittle materials indicate a less than accurate correlation of the predicted versus the actual spall strength values. It can be seen that the model significantly overpredicts the

theoretical spall strength values for ductile alloys, while it underpredicts for brittle metals and alloys.

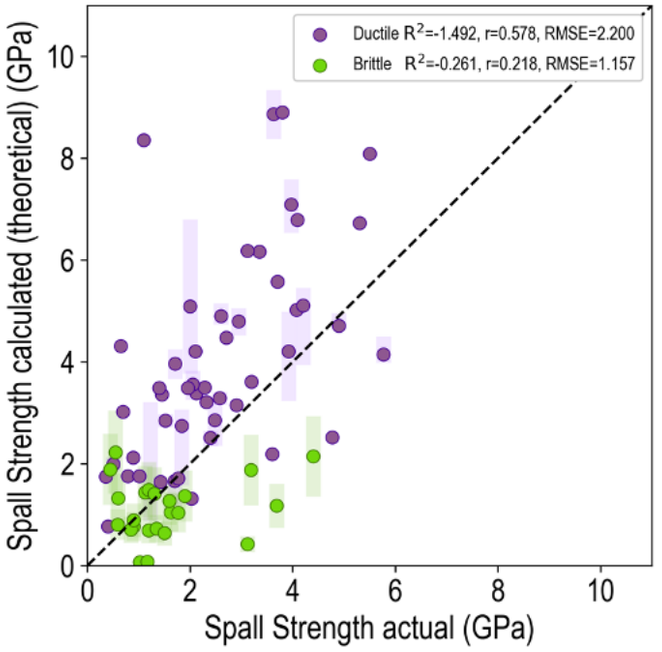

Figure 4: Results of theoretical spall strengths from Grady's ductile (purple) and brittle (green) model predictions plotted against experimental results, with vertical bars representing the range in calculated (theoretical) values.

3.2 Machine Learning Model

Figure 5(a) evaluates the performance of the developed ML model using learning curves, which show the average $RMSE$ for the train, test, and CV sets as a function of trainset size. The error bars represent one standard deviation of the average $RMSE$ values over 50 data splits, with error bars indicating the variability across these splits. As expected, the test and CV test $RMSE$ of the ML model decrease with increasing trainset size, while the train and CV train $RMSE$ increase with larger trainset size. A corresponding parity plot for the predicted and true experimental spall strength values from a single split of the 90% trainset size GPR model is shown in Figure 5(b). In this plot, the error bars for predicted values represent the standard deviation. The R^2 values for the train and test sets were 0.803 and 0.777, respectively, while the $RMSE$ values were 0.599 and 0.710, respectively. To compare experimental uncertainties with model-predicted errors, we examined 56 metals and alloys with multiple reported spall strengths, totaling 340 measurements. A histogram for deviations from the median for each material is shown in Figure S4. The measured uncertainties follow a normal distribution with a standard deviation of 0.33 GPa. Thus, the

expected range for experimental anomalies is close to the model *RMSE* values, which indicates the model is capable of capturing the noise associated with experimental spall strength measurements. Materials with the highest spall strength are more likely to deviate from the predicted values due to the fewer number of data points in that range for the model to learn from. After optimizing the hyperparameters for the train-test model, a production model was developed using 100% of the dataset for training.

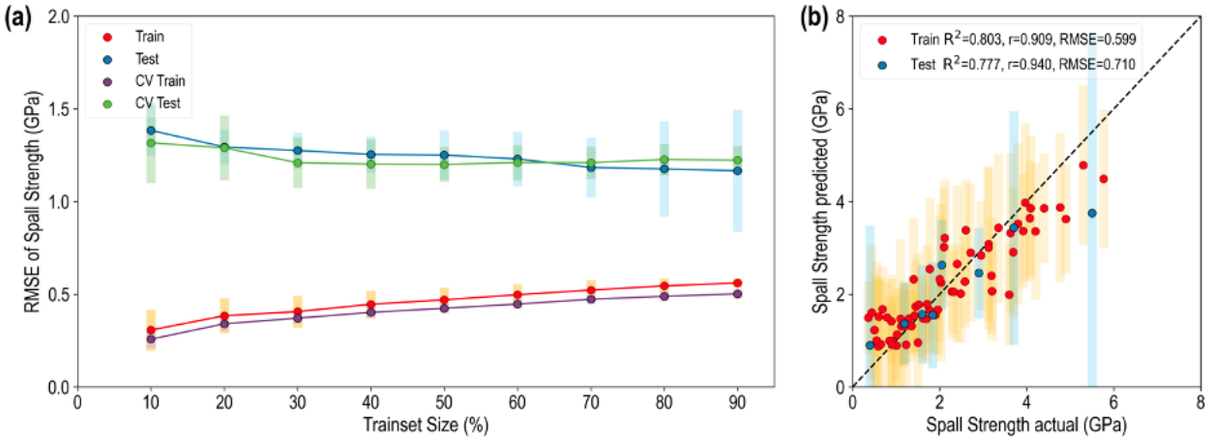

Figure 5: (a) Prediction accuracy for GPR models trained using different trainset sizes, averaged over 50 runs and (b) Parity plot for the GPR model 90-10 train-test split, with standard deviation shown as error bars, against experimental results.

3.2.1 Validation of Unseen Materials and Final Production Model

The GPR model was validated before creating the final production model, by testing with three recently investigated materials whose spall strength measurements were not included in the original training dataset. The first is a high entropy alloy, $HfZrTiTa_{0.53}$,[33] which is compositionally distinct from any other complex alloy used in the dataset. The second is the additively manufactured titanium alloy Ti-5553.[34] The third is a tungsten heavy alloy, 93WHA,[35] which is compositionally similar to a material already included in the dataset (98WHA) but has different feature values. The results of the present GPR ML production model and Grady's theoretical strength model are presented in Table 1. The GPR model predicts the spall strengths of $HfZrTiTa_{0.53}$ and 93WHA within 13% and 19%, respectively, of the experimental spall strength values (and falls within the reported range). The results for Ti-5553 are not as closely aligned with the experimental results but still fit within the reported range. For comparison, the calculated theoretical spall strengths based on Grady's model show significant discrepancies from the

experimental results, over-predicting the spall strengths for $HfZrTiTa_{0.53}$ and 93WHA and under-predicting for the Ti-5553 alloy. With the addition of these three materials, the GPR trainset was updated, and the final production model was developed.

Table 1: Features (median value) and spall strength values (experimental, theoretical as calculated by Grady's models, and predicted by the GPR model) for the validation materials.

Material	σ_{UTS} (MPa)	$\sigma_{y,tens}$ (MPa)	K (GPa)	E (GPa)	ρ (g/cm^3)	HV	K_{IC} $(MPa\sqrt{m})$	**ductile/ brittle**	$\sigma_{sp,exp}$ **(median)** (GPa)	$\sigma_{sp,Grady}$ (GPa)	$\sigma_{sp,GPR}$ (GPa)
$HfZrTiTa_{0.53}$	1110	774	110	70	9.36	372	62	ductile	2.76-3.72 (3.24)	5.05	3.65 ± 3.39
Ti-5553	769	768	82	109	4.64	413	34	brittle	3.03-4.46 (3.72)	1.74 ± 0.64	3.03 ± 2.02
93WHA	1241	920	285	368	17.61	295	41	ductile	2.40-2.73 (2.59)	8.86	3.08 ± 2.12

3.2.2 Statistical Analysis for Model Prediction

The SHapley Additive exPlanations (SHAP)[36,37] approach was used to explain statistical models by finding the importance of having a value for a feature when compared to that feature's expected value. The kernel explainer was used to compute the SHAP values for the GPR model. The highest contributing features are seen in Figure 6, revealing that tensile yield strength, bulk modulus, and Young's modulus are the three most significant features for the model. Notably, tensile yield strength emerges as the most influential feature, indicating that the spall strength is significantly affected by the quasi-static tensile yield strength. Therefore, compressibility associated with shock compression and the resistance to plastic deformation are shown to be important features that correlate best with the spall strength of the material. Fracture toughness does not serve as a primary factor. This could be associated with the fact that spall failure occurs via void nucleation and growth processes that are influenced more by strength properties.

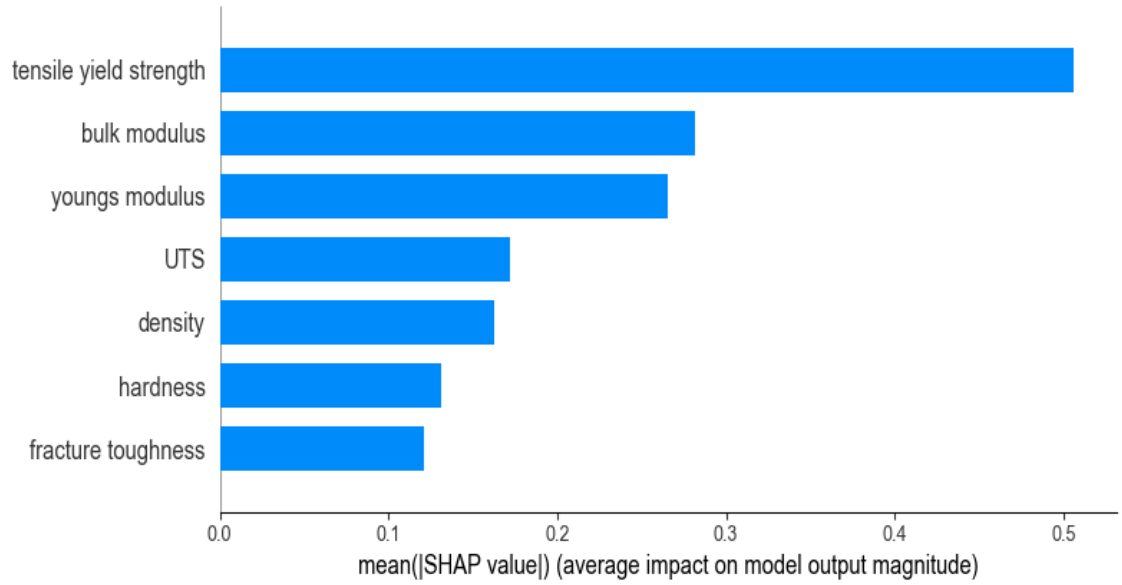

Figure 6: Feature importance based on SHAP analysis with the mean absolute SHAP values illustrating global feature importance.

3.3 Reliability and Applicability for Different Classes of Materials

The dataset of spall strength and features considered in this study comprises of various types/classes of metals and alloys, and we aimed to evaluate the performance of the final production model across the different material categories. We also sought to determine whether a correlation exists between the number of instances in a material category and lower error metrics. The average GPR standard deviation is calculated as the mean of the standard deviation values for

each material within a category. The $RMSE$ is computed by comparing the GPR-predicted spall strength to the median experimental spall strength. Additionally, the CV train and test $RMSE$ are derived from the average and standard deviation of 50 iterations of 3-fold CV runs.

Table 2 summarizes the average GPR standard deviation, $RMSE$, and CV train and test errors for the final production model across different categories of metals and alloys. The average GPR standard deviation in spall strength value across all categories is approximately 1.2 GPa. Notably, the model's performance is consistent for both pure metals and alloys, with an $RMSE$ around 0.5 GPa. Interestingly, despite having only two instances, the chromium-based alloy category demonstrates the lowest $RMSE$ value. The categories for tungsten-, magnesium-, and aluminum-based metals and alloys also show $RMSE$ values below 0.35 GPa. The iron and steels category, which has the highest number of instances, exhibits the next lowest $RMSE$ value. The average CV train and test $RMSE$ values are 1.3 GPa, with magnesium—despite having only four instances—showing significantly lower values than other material categories. Overall, the data in Table 2 indicates that there is no correlation between the increasing number of instances in a material category and improved model performance.

Table 2: Average GPR standard deviation, RMSE, and CV RMSE values of different categories of materials from the final production model that includes the validation materials.

Material Category	# of instances	average GPR stdev (GPa)	RMSE (GPa)	CV train RMSE (GPa)	CV test RMSE (GPa)
All metals & alloys	76	1.197	0.566	1.349 ± 0.037	1.406 ± 0.071
Only metals	20	1.262	0.582	1.331 ± 0.036	1.446 ± 0.117
Only alloys	56	1.174	0.560	1.355 ± 0.045	1.390 ± 0.085
Aluminum	13	0.829	0.337	1.040 ± 0.082	1.147 ± 0.270
Cobalt	2	1.161	0.815	1.176 ± 0.096	1.104 ±0.251
Chromium	2	1.564	0.188	1.063 ± 0.177	1.339 ±0.312
Copper	8	0.882	0.624	1.167 ± 0.157	1.214 ± 0.263
Iron and Steels	16	1.198	0.607	1.707 ± 0.082	1.793 ± 0.150
Magnesium	4	0.992	0.309	0.335 ± 0.074	0.345 ±0.075
Nickel	6	1.358	0.709	1.646 ± 0.076	1.583 ± 0.193
Titanium	5	1.371	0.905	1.510 ± 0.037	1.521 ± 0.169
Tungsten	4	1.581	0.339	1.228 ± 0.041	1.253 ± 0.131

3.3.1 Insights into Materials Classes

The experimental and GPR-predicted spall strengths of specific material categories are plotted in Figures 7-12 to obtain insights on observable trends of influential alloy characteristics. For pure metals (both polycrystalline and single crystal), experimental spall strength values (shown

in Figure 7) range from a low of 0.40 GPa for Ce-fcc, closely matching the GPR prediction, to a high of 4.77 GPa for Ta-bcc, which shows a larger deviation from the GPR prediction. It can be inferred that bcc and hcp metals generally have higher spall strengths than fcc metals, though there are examples of opposing trends on both sides. Aluminum and its alloys have spall strength values that are consistently among the lowest, in the range of 0.60 to 1.90 GPa as shown in Figure 8, with close correlation between experimental and GPR predictions. Interestingly, Al-2024, with three different heat treatments, shows both the lowest and highest spall strength values among all Al alloys considered, though these differences fall within the standard deviation range. For Cu-based systems (Figure 9), the ternary GRCop alloy containing Cr and Nb exhibits a higher spall strength than the binary systems. In the immiscible Cu-Ta and Cu-Pb systems, however, the GPR model predictions are higher than the experimental values. Fe-based alloys (Figure 10) exhibit the widest range of spall strength values, with minimal differences between GPR-predicted and experimental values. Complex alloy steels generally display higher spall strengths (5.30 to 5.77 GPa) compared to pure Fe and low-carbon steels (1.71 GPa). Ni-based alloys (Figure 11) exhibit no clear dominant characteristics affecting spall strength. Intermetallic compounds show contrasting trends: the B2-NiTi alloy has a spall strength nearly four times that of $L1_2$-Ni_3Al, while fcc-based complex alloys display similar differences compared to pure Ni and the Ni-60Co solid solution alloy. Overall, experimental and GPR-predicted values for Ni-based alloys are generally comparable. Lastly, Ti-based alloys (Figure 12) display a narrow range of spall strength variation, though commercial purity Ti shows a significant deviation between GPR-predicted and experimental values.

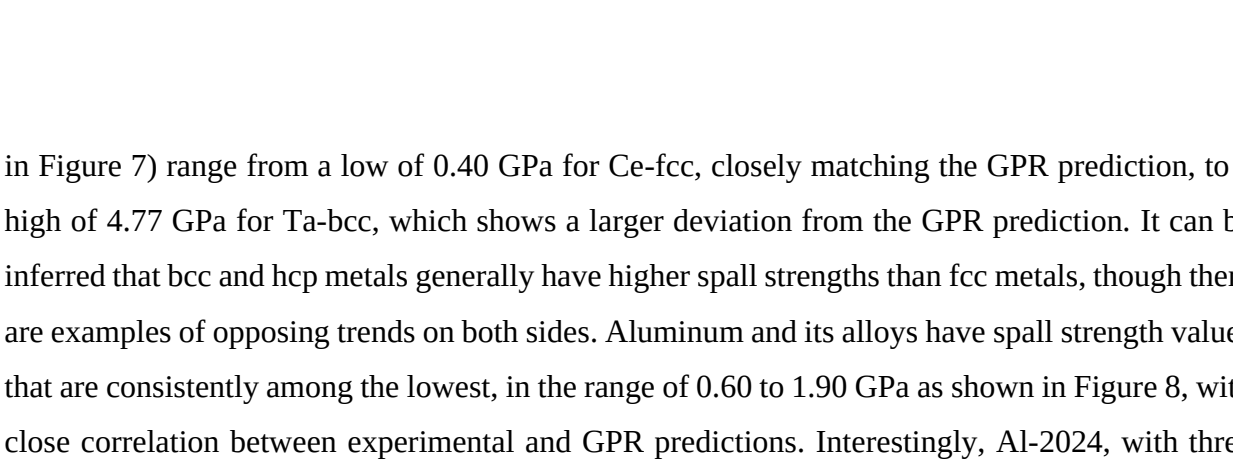

Figure 7: Median experimental spall strength of elemental metals (blue). The vertical bars indicate the range of values for those with multiple data sources. And GPR spall strength

(orange) values for each of the materials. The vertical bars indicate the standard deviation in the GPR prediction.

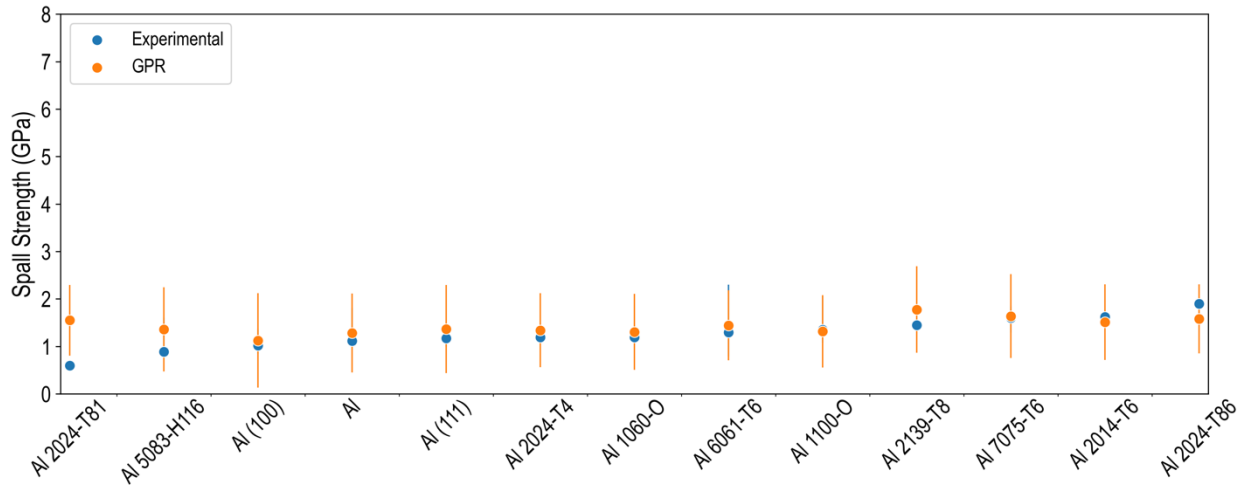

Figure 8: Median experimental spall strength of aluminum and aluminum alloys (blue). The vertical bars indicate the range of values for those with multiple data sources. And GPR spall strength (orange) values for each of the materials. The vertical bars indicate the standard deviation in the GPR prediction.

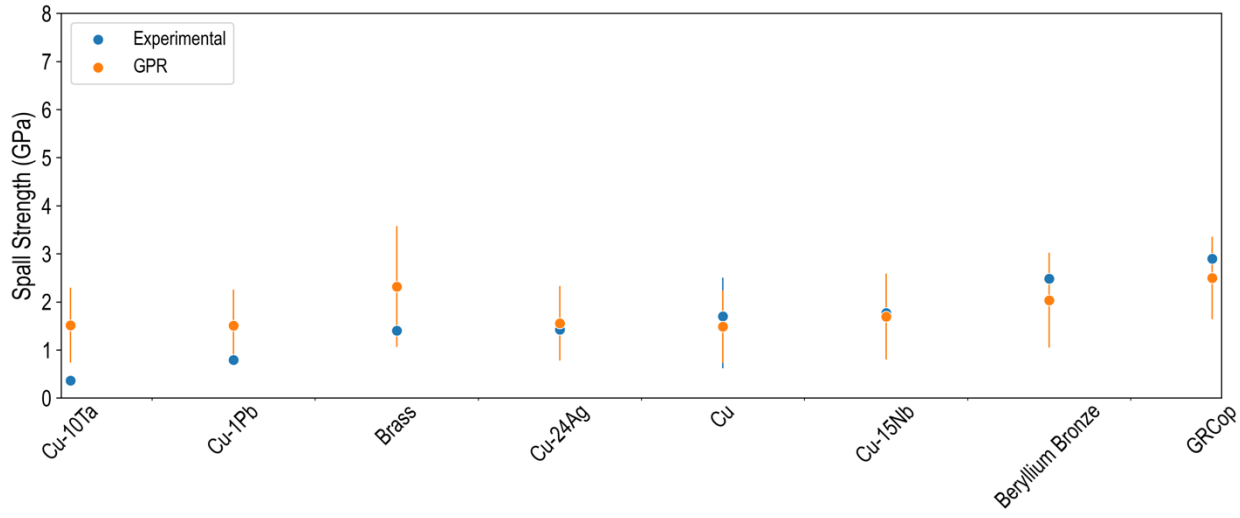

Figure 9: Median experimental spall strength of copper and copper alloys (blue). The vertical bars indicate the range of values for those with multiple data sources. And GPR spall strength (orange) values for each of the materials. The vertical bars indicate the standard deviation in the GPR prediction.

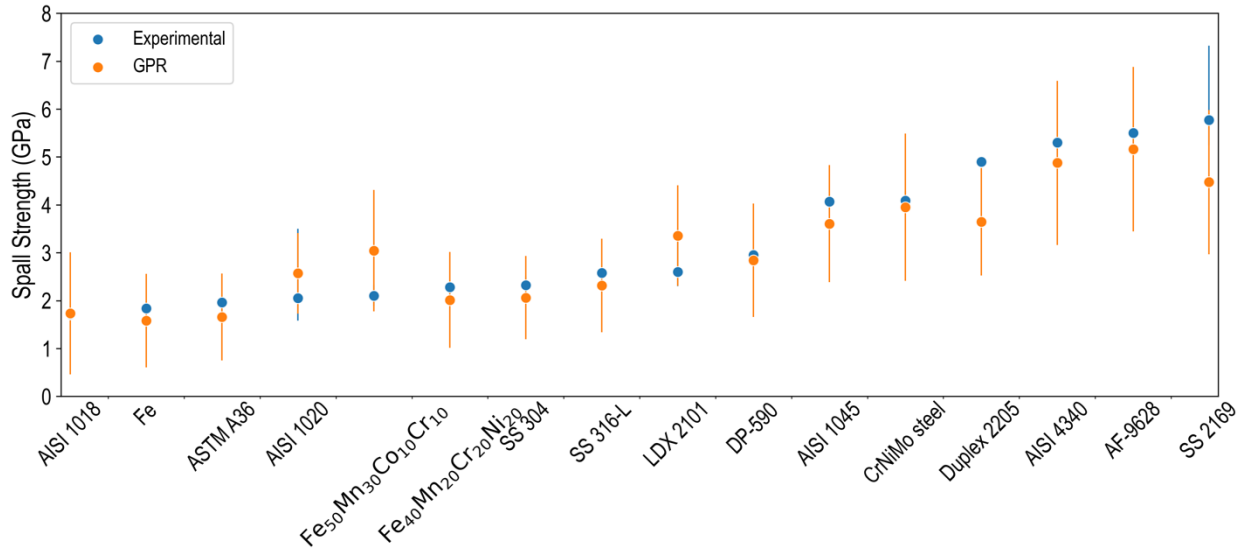

Figure 10: Median experimental spall strength of iron and steels (blue). The vertical bars indicate the range of values for those with multiple data sources. And GPR spall strength (orange) values for each of the materials. The vertical bars indicate the standard deviation in the GPR prediction.

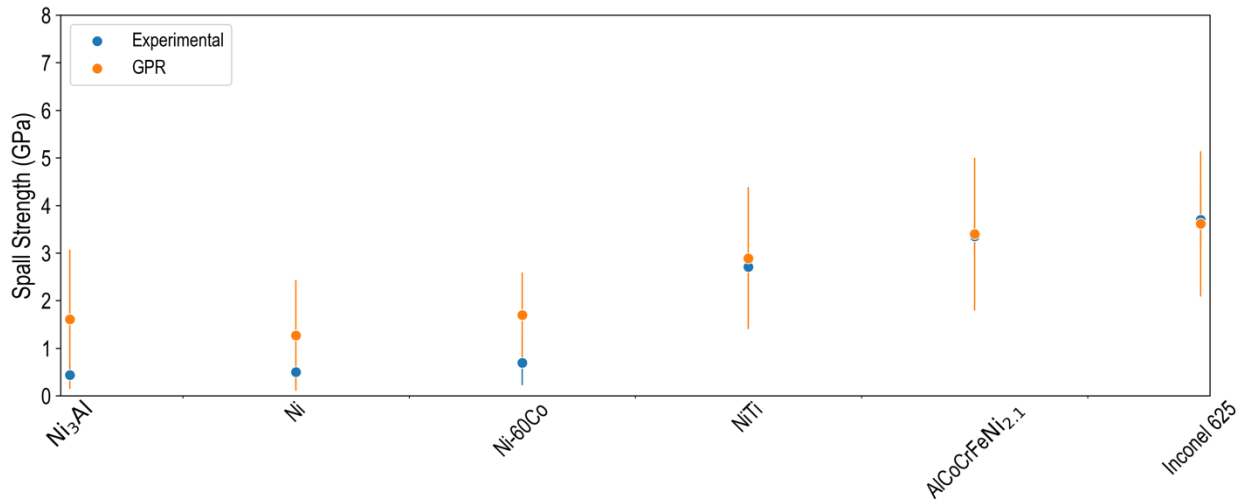

Figure 11: Median experimental spall strength of nickel and nickel alloys (blue). The vertical bars indicate the range of values for those with multiple data sources. And GPR spall strength (orange) values for each of the materials. The vertical bars indicate the standard deviation in the GPR prediction.

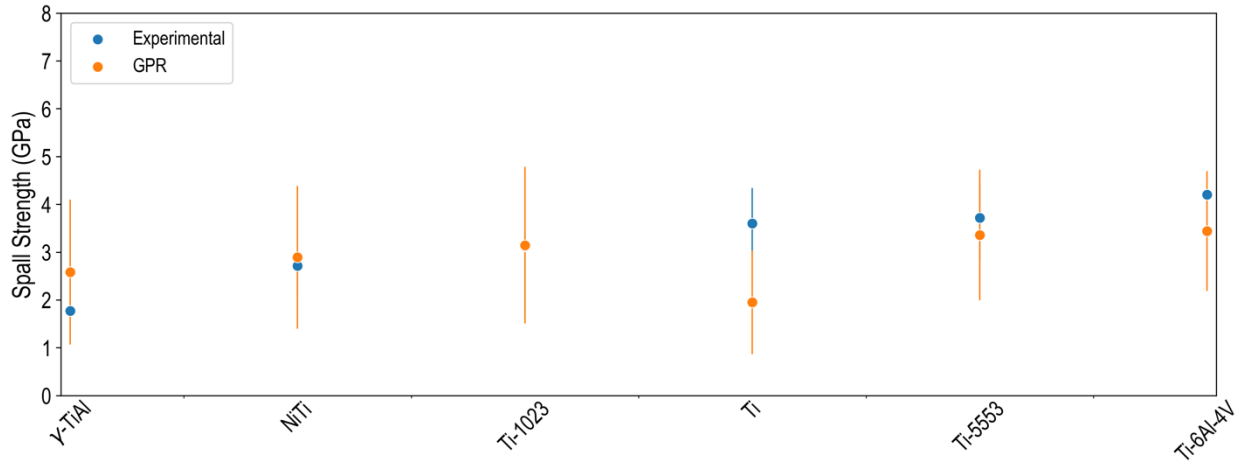

Figure 12: Median experimental spall strength of titanium and titanium alloys (blue). The vertical bars indicate the range of values for those with multiple data sources. And GPR spall strength (orange) values for each of the materials in the dataset. The experimental point for Ti-1023 is overlapped by the GPR data point. The vertical bars indicate the standard deviation in the GPR prediction.

3.3.2 Predicting Spall Strengths for New Alloys

High entropy alloys (HEAs), also known as complex alloys containing five elemental components often as a single-phase solid solution, generally exhibit superior mechanical properties compared to conventional alloys.[38] However, these alloys are relatively understudied in the context of their high-strain-rate mechanical behavior. The GPR model was employed to screen several instances of this alloy class. Currently, only eight HEAs have documented spall strengths along with the requisite seven features as reported in the literature. These eight HEAs are already included in the model's trainset. Mechanical property data corresponding to the required features recently reported in the literature were gathered for six additional HEAs, though their experimental spall strengths are unavailable. The GPR model was utilized to predict the spall strength for each HEA, and the complete set of their predicted values and features is presented in Table 3. As noted in the table, while most HEAs are single-phase solid solutions, dual-phase alloys have also been recently investigated. Figure 13 shows a plot of the experimental and GPR predicted spall strength values of the eight HEAs, along with the GPR-predicted values of the six HEAs for which their experimental values are not reported. The predictions for the GPR model for this latter group of HEAs shows a higher standard deviation which we attribute to their not being included in the trainset of model development. In general, it is seen that the experimental spall strengths of fcc-

based HEAs are generally lower than bcc-based HEAs, except for $Al_{0.1}CoCrFeNi$, though in all cases, the HEAs have relatively higher values of spall strength.

It is interesting to note that, as presented in section 3.3.1, aluminum and its alloys almost uniformly have low spall strength. For HEAs based on aluminum, however, the spall strength values are higher, with two of those being dual-phase alloys. Similarly, for copper and its alloys, the spall strength values of the Cu-based HEAs fall at the higher end of the range. In contrast, for iron and steels, the spall strengths of HEAs fall in between that of the plain carbon steels and alloy steels. The single-phase Hf-, Co-, and Cr-based HEAs generally have spall strength values that are in the middle-to-high range for different metals and alloys.

Overall, the predicted spall strength values for HEAs range from 1.54 to 4.13 GPa, closely aligning with their median experimental values in the model's training dataset (1.52 to 3.69 GPa). These values are at the higher end of the spall strength range for all materials considered in our dataset. Given the similarity in features and spall strength values, predictions for HEAs without reported experimental values are anticipated to be reliable, providing the impetus for future experimental validation. These results also offer guidance for designing new high-strength multi-component alloys, such as aluminum and copper-based alloys.

Table 3: Median values for the features and spall strength values (median experimental and predicted by the GPR model) for the HEAs.

Material	Crystal structure	σ_{UTS} (MPa)	$\sigma_{y,tens}$ (MPa)	K (GPa)	E (GPa)	ρ (g/cm^3)	HV	K_{IC} $(MPa\sqrt{m})$	$\sigma_{sp,exp}$ (GPa)	$\sigma_{sp,GPR}$ (GPa)
$Al_{0.1}CoCrFeNi$	fcc	531	199	172	211	7.88	458	14	3.69	2.94 ± 1.41
$AlCoCrFeNi_{2.1}$	fcc + bcc	1165	750	169	185	7.37	9	119	3.35	3.40 ± 1.61
CoCrFeNi	fcc	413	147	169	219	8.23	135	28	3.19	2.39 ± 1.26
CrMnFeCoNi	fcc	600	265	144	203	7.86	228	262	2.12	3.24 ± 1.26
FeCrNiMn	fcc	513	229	118	202	7.72	201	135	1.52	1.75 ± 1.06
$Fe_{40}Mn_{20}Cr_{20}Ni_{20}$	fcc	694	306	133	195	7.90	150	137	2.28	2.01 ± 1.00
$Fe_{50}Mn_{30}Co_{10}Cr_{10}$	fcc	763	410	144	202	6.65	259	217	2.10	3.04 ± 1.27
$HfZrTiTa_{0.53}$	bcc	1110	774	110	70	9.36	372	62	3.24	3.39 ± 1.66
AlCoCrFeNi	fcc + bcc	397	345	150	126	7.00	518	25	---	4.13 ± 2.37
$CoCrFeNiS_{0.5}$	fcc	2320	556	138	166	7.19	259	22	---	3.29 ± 4.03
CuCrFeTiZn	fcc + bcc	1436	585	201	241	6.94	655	22	---	1.98 ± 3.59
$(CuCrFeTiZn)_{90}Pb_{10}$	fcc + bcc	1151	258	120	144	7.85	418	10	---	1.54 ± 3.03
$(CuCrFeTiZn)_{95}Pb_5$	fcc + bcc	856	440	145	174	7.55	530	13	---	2.93 ± 2.26
HfNbTaTiZr	bcc	957	875	148	98	9.72	295	210	---	4.02 ± 3.72

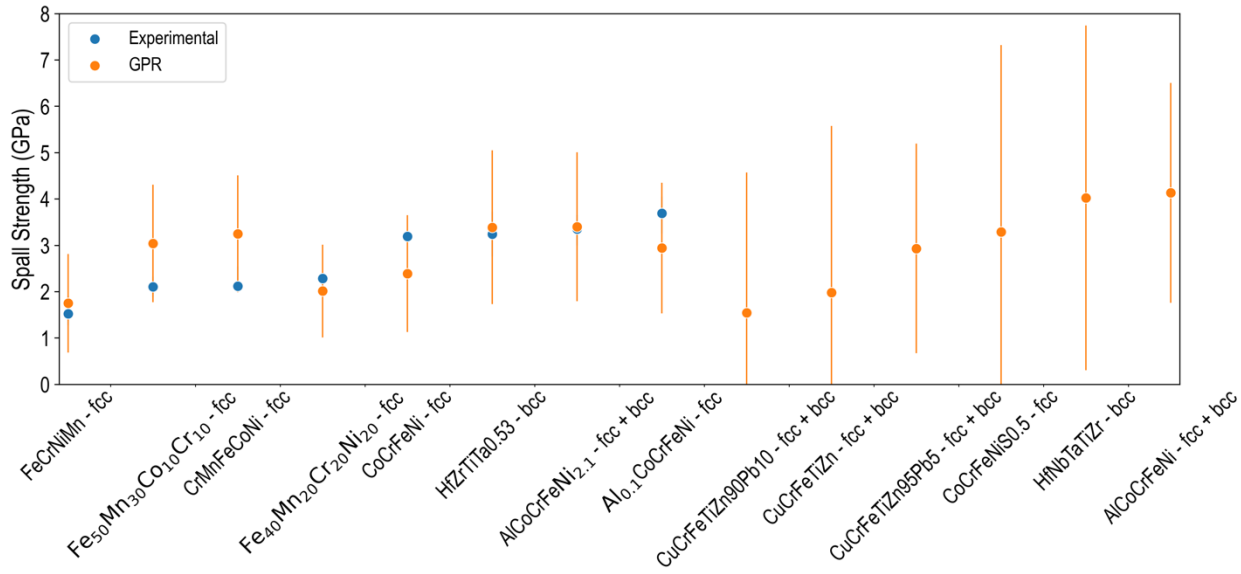

Figure 13: Median experimental spall strength of HEAs for which there are values available (blue). The vertical bars indicate the range of values for those with multiple data sources. And GPR spall strength (orange) values for each of the materials. The vertical bars indicate the standard deviation in the GPR prediction.

Based on the results reported in this work, it can be seen that, in general, Grady's model for prediction of the theoretical spall strength generally overpredicts spall strength values compared to their experimental values as reported in the literature, especially for ductile metals and alloys. As an advantage, however, it requires minimal material properties as inputs. The GPR model, on the other hand, while needing seven features, is able to predict spall strength values that are closer to the experimentally measured values for a wide range of metals and alloys. Though the GPR model does not explicitly account for the microstructure, the properties considered relate to material compressibility and strength that are implicitly related to the microstructural effects. Future work can potentially incorporate microstructural characteristics, including phases present and their crystal structure, grain size, volume fraction, etc. Further correlation of the microstructure with processing conditions would enable pathways for tailoring spall strength properties for desired performance requirements or applications.

4. Conclusions

In this study, a Gaussian Process Regression (GPR) model was developed to predict the spall strengths of metals and alloys, trained on a dataset of over 70 materials. Validated on three recently reported materials, the model accurately predicted spall strength, underscoring its reliability.

Model analysis identified tensile yield strength and bulk modulus as the most important features for predicting spall strength, with higher values correlating to stronger spall strengths. Although fracture toughness improves model accuracy, it is not a primary factor influencing spall strength, which is more controlled by strength properties governing void nucleation and growth. However, removing it significantly reduces model performance. The model successfully predicted spall strengths for known high entropy alloys (HEAs) and made predictions for untested HEAs. A Colab notebook, accessible to non-experts, installs dependencies and enables rapid spall strength predictions across a range of metals and alloys, offering a valuable tool for the research community.

Supplementary Material

The provided supplementary material includes additional data and analyses supporting the findings in the main text. Key components include: (1) Median spall strengths and related properties of metals and alloys, (2) Linear regression parity plot illustrating model accuracy, (3) Correlation plots showing relationships among features, (4) Feature selection criteria and rationale, and (5) Estimations of experimental uncertainties for spall strength measurements across multiple samples.

Conflict of Interest

The authors have no conflicts to disclose.

Author Contributions

KGF: Methodology (lead); writing – original draft (lead); formal analysis (lead); writing – review and editing (equal). **NNT**: review and editing (equal). **RR**: review and editing (equal). **HS**: Methodology (support); review and editing (equal).

Acknowledgements

This work was supported in part by the U.S. Army Research Office Cooperative Agreement Project No. W911NF-24-2-0116 and the Georgia Tech Foundation funds. KGF acknowledges the graduate fellowship funding provided by Department of Defense (DoD) through the National Defense Science & Engineering Graduate (NDSEG) Fellowship Program.

Data Availability Statement

All data supporting the findings of this study are accessible on GitHub at https://github.com/Ramprasad-Group/spall_strength_prediction. The repository includes the code, dataset, and a Colab notebook that installs all dependencies and uses our predictive model to estimate spall strength based on seven features: ultimate tensile strength, tensile yield strength, fracture toughness, hardness, density, bulk modulus, and Young's modulus. It also generates plots to visualize the spall strength dataset.

References

1. Meyers, M. A. & Aimone, C. T. Dynamic fracture (spalling) of metals. *Prog. Mater. Sci.* **28,** 1; 10.1016/0079-6425(83)90003-8 (1983).
2. Antoun, T. et al. *Spall Fracture*; 10.1007/b97226 (Springer, 2003).
3. Meyers, M.A. *Dynamic Behavior of Materials*; 10.1002/9780470172278 (John Wiley & Sons, Inc., 1994).
4. Grady, D.E. & Kipp, M.E. Dynamic Fracture and Fragmentation in *High-Pressure Shock Compression of Solids* (eds. Asay, J.R. & Shahinpoor, M.) 265-322; 10.1007/978-1-4612-0911-9_8 (Springer, 1993).
5. Curran, D.R., Seaman, L. & Shockey, D.A. Dynamic failure of solids. *Phys. Rep.* **147,** 5; 10.1016/0370-1573(87)90049-4 (1987).
6. Lloyd, J. T. et al. Manipulating shock waves with metallurgy. *Acta Mater.* **234,** 118042; 10.1016/j.actamat.2022.118042 (2022).
7. Fensin, S.J. et al. Effect of grain boundary structure on plastic deformation during shock compression using molecular dynamics. *Model. Simul. Mater. Sci. Eng.* **21,** 015011; 10.1088/0965-0393/21/1/015011 (2013).
8. Flanagan, R.M., Fensin, S.J. & Meyers, M.A. The role of pre-existing heterogeneities in materials under shock and spall. *Appl. Phys. Rev.* **9,** 011305; 10.1063/5.0053693 (2022).
9. Kanel, G.I. Spall fracture: methodological aspects, mechanisms and governing factors. *Int. J. Fract.* **163,** 173-191; 10.1007/s10704-009-9438-0 (2010).
10. Neel, C., Gibbons, S., Abrahams, R. & House, J. Shock and Spall in the Low-alloy Steel AF9628. *J. Dyn. Behav. Mater.* **6,** 64-77; 10.1007/s40870-019-00228-5 (2020).
11. Huang, S., Jin, X., Li, Z., Wang, X. & Guan, K. Experimental measurements of 2169 stainless steel under dynamic loading. *AIP Conf. Proc.* **309,** 1083-1086; 10.1063/1.46293 (1994).
12. Grady, D. E. The spall strength of condensed matter. *J. Mech. Phys. Solids* **36,** 353-384; 10.1016/0022-5096(88)90015-4 (1988).
13. Cochran, S. & Banner, D. Spall studies in uranium. *J. Appl. Phys.* **48,** 2729-2737; 10.1063/1.324125 (1977).
14. Chen, D. et al. A modified Cochran–Banner spall model. *Int. J. Impact Eng.* **31,** 1106-1118; 10.1016/j.ijimpeng.2004.07.007 (2005).
15. Xiong, J., Zhang, T. & Shi, S. Machine learning of mechanical properties of steels. *Sci. China Technol. Sci.* **63,** 1247-1255; 10.1007/s11431-020-1599-5 (2020).
16. Stoll, A. & Benner, P. Machine learning for material characterization with an application for predicting mechanical properties. *GAMM-Mitteilungen* **44,** e202100003; 10.1002/gamm.202100003 (2021).
17. Agrawal, A. et al. Exploration of data science techniques to predict fatigue strength of steel from composition and processing parameters. *Integrating Mater. Manuf. Innov.* **3,** 90-108; 10.1186/2193-9772-3-8 (2014).
18. Mayer, P. N., Pogorelko, V. V., Voronin, D. S. & Mayer, A. E. Spall fracture of solid and molten copper: Molecular dynamics, mechanical model and strain rate dependence. *Metals* **12,** 1878; 10.3390/met12111878 (2022).
19. Mayer, A. E., Lekanov, M. V., Grachyova, N. A. & Fomin, E. V. Machine-learning-based model of elastic-plastic deformation of copper for application to shock wave problem. *Metals* **12,** 402; 10.3390/met12030402 (2022).

20. Blaschke, D.N., Nguyen, T., Nitol, M., O'Malley, D. & Fensin, S. Machine learning based approach to predict ductile damage model parameters for polycrystalline metals. *Comput. Mater. Sci.* **229,** 112382; 10.1016/j.commatsci.2023.112382 (2023).
21. Mayer, A.E. Influence of preliminary compressive deformation on the spall strength of aluminum single crystal. *Scripta Materiala*. **242**, 115905; 10.1016/j.scriptamat.2023.115905 (2024).
22. Rasmussen, C. E. & Williams C. K. I. *Gaussian Processes for Machine Learning* (MIT Press, 2006).
23. Boddorff, A.K., Jang, S., Kennedy, G., Taminger, K. & Thadhani, N. N. Spall failure of additively manufactured two-layered Cu–Ni bimetallic alloys. *J. Appl. Phys.* **131,** 175901; 10.1063/5.0086445 (2022).
24. Whelchel, R.L., Sanders, T.H. & Thadhani, N.N. Spall and dynamic yield behavior of an annealed aluminum–magnesium alloy. *Scr. Mater.* **92,** 59-62; 10.1016/j.scriptamat.2014.08.014 (2014).
25. Whelchel, R. L., Mehoke, D. S., Iyer, K. A., Sanders, T. H. & Thadhani, N. N. Dynamic yielding and fracture of grade 4 titanium in plate impact experiments. *J. Appl. Phys.* **119,** 115901; 10.1063/1.4943777 (2016).
26. Mallick, D. D. et al. Laser-driven flyers and nanosecond-resolved velocimetry for spall studies in thin metal foils. *Exp. Mech.* **59,** 611-628; 10.1007/s11340-019-00519-x (2019).
27. Chen, X. et al. Spallation of polycrystalline tungsten using laser-induced shock at ultrahigh strain rates. *Int. J. Impact Eng.* **166,** 104243; 10.1016/j.ijimpeng.2022.104243 (2022).
28. Curran, D. R., Seaman, L. & Shockey, D. A. Dynamic failure in solids. *Phys. Today* **30,** 46-55; 10.1063/1.3037367 (1977).
29. Ford, H. The tensile properties of metals. *RSA* **103,** 471; https://www.proquest.com/scholarly-journals/tensile-properties-metals/docview/1307293799/se-2?accountid=11107 (1955).
30. Pedregosa, F. et al. Scikit-learn: Machine learning in Python. *J. Mach. Learn. Res.* **12,** 2825-2830; https://www.jmlr.org/papers/volume12/pedregosa11a/pedregosa11a.pdf (2011).
31. Tran, H. D. et al. Machine-learning predictions of polymer properties with Polymer Genome. *J. Appl. Phys.* **128,** 171104; 10.1063/5.0023759 (2020).
32. Hastie, T., Tibshirani, R. & Friedman, J. *The Elements of Statistical Learning: Data Mining, Inference, and Prediction* 10.1007/978-0-387-84858-7 (Springer, 2009).
33. Zhang, N. B. et al. Orientation relationships of impact-induced phase transformation in high entropy alloy HfZrTiTa0.53. *Scr. Mater.* **244,** 116007; 10.1016/j.scriptamat.2024.116007 (2024).
34. Specht, P. E. et al. Dynamic response of additively manufactured Ti–5Al–5V–5Mo–3Cr as a function of heat treatment. *J. Appl. Phys.* **135,** 055901; 10.1063/5.0181340 (2024).
35. Xiang, Y., Chen, S., Li, Z., Yu, Y. & Hu, J. Spallation damage of tungsten heavy alloy under shock loading. *Mater. Lett.* **360,** 135977; 10.1016/j.matlet.2024.135977 (2024).
36. Lundberg, S. & Lee, S. I. A unified approach to interpreting model predictions. *NIPS* 10.48550/arXiv.1705.07874 (2017).
37. Lundberg, S. M. et al. From local explanations to global understanding with explainable AI for trees. *Nat. Mach. Intell.* **2,** 56-67; 10.1038/s42256-019-0138-9 (2020).
38. George, E.P., Raabe, D. & Ritchie, R.O. High-entropy alloys. *Nat Rev Mater*. **4,** 515-534; 10.1038/s41578-019-0121-4 (2019).